Characterization of Electric Field Distribution Within High Voltage Press-packed IGBT Submodules Under Conditions of Repetitive Turn-on and Turn-off

Teng Wen, Xiang Cui, *Senior Member*, *IEEE*, *Fellow*, *CSEE*, Sijia Liu, Xuebao Li, *Member*, *IEEE*, *Member*, *CSEE*, and Zhibin Zhao, *Member*, *IEEE*

***Abstract*—The high-voltage high-power press-packed IGBT (PPI) devices are the key component of the DC transmission apparatus. A PPI device is composed of several PPI submodules. In general, the PPI submodule works in a state of repetitive turn-on and turn-off, and the corresponding working voltage is the positive periodic square waveform (PPSW) voltage, which is much different from the conventional AC or DC voltage. In addition, insulation capability is one of the most critical challenges in the design and fabrication of PPI devices. To improve the insulation capability of the device, composite insulation structures with multiple dielectrics are usually employed. Under the PPSW voltage, it is essential to analyze the transient electric field to solve the insulation challenge of the PPI devices. However, the electric field of the PPI is often calculated under the electrostatic field or DC field. Moreover, the transient characteristics of the electric field are ignored. Therefore, this paper focuses on the analysis of the transient characteristics of the electric field of the PPI submodule under the PPSW voltage. The influences of the waveform parameters of the PPSW voltage on the transient characteristics are demonstrated in detail. This study is significant for the insulation analysis and design of the PPIs.**

***Index Terms*—Electroquasistatic field, FEM, IGBT, positive periodic square waveform voltage, transient electric field.**

I. Introduction

With the rapid development of renewable energy and the application of DC transmission technology, various types of power electronic devices with high voltage and large capacity have been widely used in the power grid [1], [2]. The high-voltage and high-power insulated gate bipolar transistor (IGBT) is the key component of the electrical apparatus for power conversion and control [3], [4]. In general, high-voltage IGBT devices can be classified into two types, wire-bonded IGBT (WBI) modules and press-packed IGBT (PPI) devices, according to their packaging types [5], [6]. Compared with WBI modules, PPI devices have the advantages of double-sided heat dissipation, short-circuit failure mode, and easy parallel connection, which makes them a more suitable choice for practical power application [6].

In general, a PPI device is composed of several IGBT submodules and fast recovery diode (FRD) submodules in parallel to obtain the required current rating, as shown in Fig. 1(a). As depicted in Fig. 1(b), a submodule consists of an IGBT/FRD die, upper and lower molybdenum pads, a silver plate, and a polyetheretherketone (PEEK) frame. The die is sandwiched between upper and lower molybdenum pads, and the submodule is mounted on the pillar electrode. In the IGBT submodule, a spring pin is employed to connect the gate of the IGBT die with the outer gate electrode on the ceramic hermetic package. After the submodules are mounted onto the pillar electrodes, the PPIs are sealed with pressurized protective gas, which is often nitrogen. In the PPIs, all the electrical contacts are achieved only by clamping forces [7].

Briefly, the insulation structure of the submodule is a typical composite insulation structure composed of a passive layer, protective gas, and a PEEK frame [7]. In addition, the shape of the submodule is a cube with a dimension of 1 centimeter, which is quite small. Therefore, under the working voltage, the high electric field will be produced in the submodule. The local reinforced electric field at the insulation structure will cause partial discharge, and then weaken the insulation property of the insulation structure, which might even lead to an electric breakdown [8]–[10]. As a result, electrical insulation capability is one of the most critical challenges in the design and fabrication of PPIs. To understand the insulation failure mechanism and solve the insulation problem, it is fundamental to analyze the distribution of the electric field inside the submodule. Consequently, a thorough understanding of the characteristics of the electric field of the PPI submodule is imperative.

From a general perspective, the PPI device works in a state of repetitive turn-on and turn-off in applications, such as DC transmission apparatus [11], [12], pulse power [13],

Manuscript received February 24, 2021; revised May 30, 2021; accepted July 26, 2021. Date of online publication January 5, 2022; date of current version February 19, 2022. This work was supported by the National Natural Science Foundation of China-State Grid Corporation Joint Fund for Smart Grid (No. U1766219).

T. Wen (ORCID: https://orcid.org/0000-0002-8371-5161), X. Cui, S. J. Liu, X. B. Li (corresponding author, e-mail: lxb08357x@ncepu.edu.cn), and Z. B. Zhao are with State Key Laboratory of Alternate Electrical Power System with Renewable Energy Sources, North China Electric Power University, Beijing 102206, China.

DOI: 10.17775/CSEEJPES.2021.01390

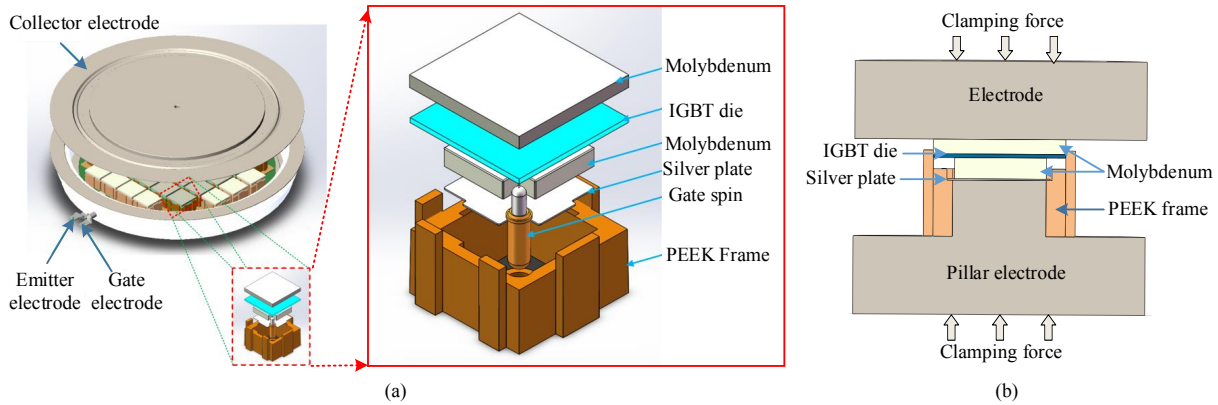

Fig. 1. Schematic of PPIs. (a) Explosive view of PPI device. (b) Cross-section of the PPI submodule [7].

PWM inverter fed motor [14], and etc. The working voltage resisted by the device is the positive periodic square waveform (PPSW) voltage, which is much different from the traditional AC or DC voltage. Under the PPSW voltage, the charge relaxation phenomena should be considered due to the discontinuity of the permittivity of the different materials in the composite insulation structure of the PPI submodule [15]. Consequently, the calculation of the transient electric field of the submodule under the above working state should follow the electroquasistatic (EQS) field equations [16]. For the composite insulation structure, the maximum electric field often occurs on the surface of the conductor or the dielectric interface where the normal component of the electric field is discontinuous [17]. Therefore, the electric field on the conductor surface and dielectric interface should be calculated with higher accuracy [18].

To the best of our knowledge, the existing research on electric field analysis of the packaging insulation structure of IGBTs primarily aims at the WBIs [19]–[22], especially the triple point of mental, ceramic, and silicone gel [23]–[25]. By contrast, the knowledge of electric field analysis for PPIs is much less mature with few pieces of literature published. In addition, these analyses of the electric field are often conducted under the electrostatic field [7], [26], or DC field [27], without considering the working state of the repetitive turn-on and turn-off. Recently, the electric field analysis of the substrate for wire-bonded power electronics was conducted under the bipolar square waveform voltage with a frequency of 200 Hz. However, the transient characteristics of the electric field were not revealed [28]. In summary, under the PPSW voltage, a comprehensive analysis of the temporal and spatial distribution characteristics of the transient electric field considering the working state of repetitive turn-on and turn-off is paramount.

This paper focuses on the transient electric field analysis of the PPI submodule under the condition of repetitive turn-on and turn-off. First, the calculation model is introduced, and the boundary condition of the calculation model is illustrated. Secondly, the initial-boundary value problem is described, and the FEM in time-domain is introduced, by which the electric field on the conductor surface and dielectric interface can be calculated with high accuracy. Thirdly, the temporal and spatial distribution characteristics of the transient electric field are comprehensively analyzed under the PPSW voltage. Finally, the influence of the duty cycle and the cycle of the PPSW voltage on the transient electric field is analyzed. The results show that not only the modulus of the electric field changes transiently but also the location of the maximum electric field transfer varies with time, which cannot be obtained by static analysis or steady-state analysis. This study is helpful for the insulation analysis and design of the PPIs.

II. Numerical Model for Calculation

A. Numerical Model of the PPI Submodule

The model of the submodule for electric field calculations is presented in Fig. 2. In the model, a 2-D parallel plane model is selected to simplify the calculation. Due to the symmetry of the structure, the right part of the cross-section is selected for the calculation. The die is sandwiched by the molybdenum after the clamping force is applied. The molybdenum is electrically connected to the pillar electrode via the silver plate. The PEEK frame is in contact with the pillar electrode and silver plate. The remaining areas are filled with nitrogen.

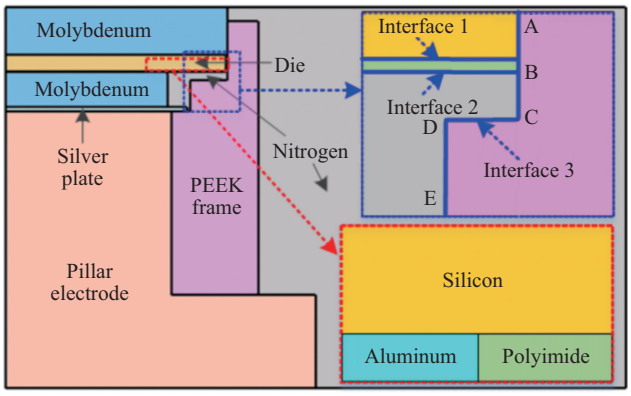

Fig. 2. The 2-D model of PPI submodule for calculation.

The composite insulation structure of the submodule is composed of polyimide, PEEK, and nitrogen. There are three dielectric interfaces in the composite insulation structure, the interface between silicon and polyimide, the interface between

polyimide and nitrogen, the interface between PEEK and nitrogen, which are marked with blue lines, and simplified as interface 1, interface 2, and interface 3 in Fig. 2.

As for the die model, since the electric field distribution at the periphery of the die is primarily determined by the termination and passivation structures of the die, a simplified die model may be used as in [29]. In our model, the die is simplified as material silicon, and the passive layer is primarily made of polyimide. The basic parameters of the material are summarized in Table I. The relative permittivity and conductivity of PEEK and polyimide are determined by experiments in our laboratory, while for the silicon and nitrogen, the relative permittivity and conductivity are in [27].

TABLE I
BASIC PARAMETERS OF THE MATERIALS

Material	Relative permittivity	Conductivity (S/m)
PEEK	3.93	2.55×10^{-15}
polyimide	2.96	4×10^{-14}
silicon	11.7	2.5×10^{-4}
nitrogen	1.0	1×10^{-11}

B. Initial Value-boundary Value Problem

To characterize the transient electric field of the package insulation structure of the submodule, the EQS field needs to be considered. Under the EQS condition, the initial value and boundary value problem for scalar electric potential can be expressed as:

$$\begin{cases} \nabla \cdot \left[\gamma \nabla \varphi + \frac{\partial}{\partial t}(\varepsilon \nabla \varphi)\right] = 0 \\ \varphi|_{\Gamma_1} = U(t) \\ \frac{\partial \varphi}{\partial t}\big|_{\Gamma_2} = 0 \\ \varphi|_{t=0} = 0 \end{cases} \tag{1}$$

where ε and γ are permittivity and conductivity of the materials, respectively, Γ_1 is the Dirichlet boundary where the electric potential is given, $U(t)$ is the given function corresponding to the Dirichlet boundary, Γ_2 is the Neumann boundary where the normal component of electric potential is zero, respectively, t is time, and $\varphi|_{(t=0)}$ denotes the initial distribution of electric potential. In our model, the initial value of the potential is zero.

C. Boundary Condition of the PPI Submodule

1) Working Voltage under Conditions of Repetitive Turn-on and Turn-off

The PPI device always works under a condition of a repeated turn-on and turn-off state. Under this working condition, the PPI submodule is subjected to the positive periodic square waveform (PPSW) voltage, which is depicted in Fig. 3. Under the off-state, the submodule withstands high voltage, and the amplitude of the voltage is U_{m}, while under the on-state, the submodule does not withstand voltage. During the turn-off process, the voltage rises from 0 to U_{m}, and the rise time is t_{r}. While during the turn-on process, the voltage decrease from U_{m} to 0, and the fall time is t_{f}. The cycle of the PPSW voltage is T, and the duty cycle is α. The duty cycle is defined as the ratio of the duration of the turn-off process and off-state within a cycle to the duration of the cycle, where $0 < \alpha < 1$.

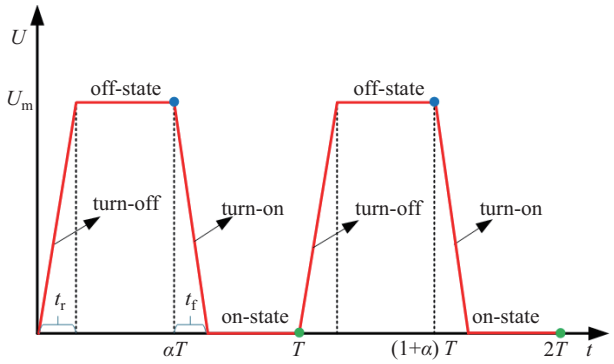

Fig. 3. Schematic of positive periodic square waveform voltage.

2) Boundary Condition

The boundary condition of the numerical model is depicted in Fig. 4. When the submodule is in the turn-off process, or in the off-state, and during the turn-on process, the boundary condition of the model is as shown in Fig. 4(a). Under this condition, the emitter and the gate of the submodule are grounded, and the high collector withstands the high potential. Therefore, the electric potential of the pillar electrode, silver plate, and the down molybdenum pad is zero, and the potential of the upper electrode and the upper molybdenum pad is high voltage. In

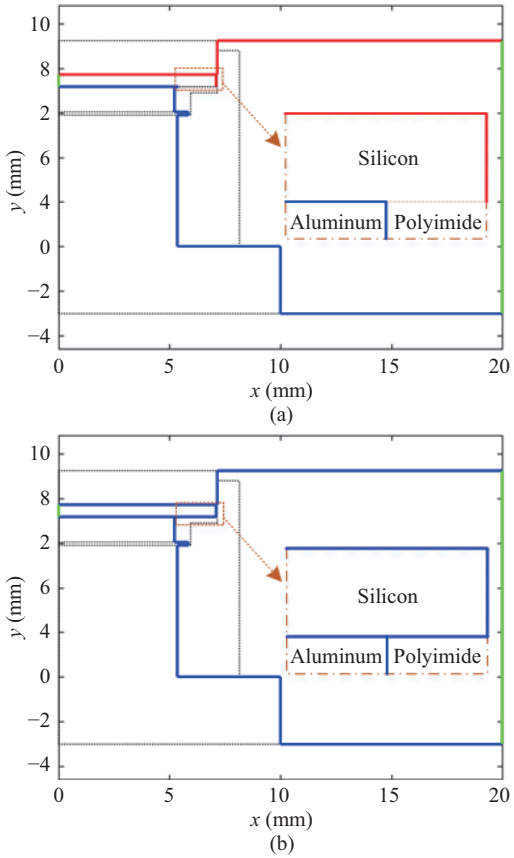

Fig. 4. Schematic of boundary condition. (a) Turn-off process, off-state, turn-on process. (b) On-state.

particular, the potential of the edge of the die is approximate as high potential according to the simulation results of the die by the TCAD simulation [29]. The left boundary of the die is the axis symmetry, and the right hand of the calculation model is assumed to be the zero flux of the electric field, which is the homogeneous Newman boundary. In Fig. 4(a), the Dirichlet boundary with high potential is depicted by red lines, the Dirichlet boundary with zero potential is depicted by blue lines, and the homogeneous Newman boundary is indicated by green lines. Thus, the field domain for calculation is the closed area formed by red lines, blue lines, and green lines.

When the submodule is in the on-state, the die is assumed to be the conductor, the boundary condition of the model is shown in Fig. 4(b). As a result, the Dirichlet boundary with high potential in Fig 4(a) is turned to be zero potential, and the periphery of the die is also the Dirichlet boundary with zero potential, which is depicted by blue lines in Fig. 4(b). The homogeneous Newman boundary indicated by green lines in Fig. 4(b) is the same as Fig. 4(a). Under this condition, the field domain is the closed area formed by blue lines and green lines.

III. Numerical Method of THE Transient Electric Field

Within the combined insulation structure, the critical area with the reinforced electric field often occurs at the surface of the conductor or the interface of the dielectrics [17]. Therefore, the calculation method for the electric field on the surface of the conductor and the dielectric interface with high accuracy is essential. The calculation method is proposed in our previous paper, in which the calculation accuracy is more than an order of magnitude higher than traditional FEM in the time domain [18]. In this paper, the proposed FEM in time-domain under the step voltage [18] is extended to the positive periodic square waveform voltage.

A. Numerical Method

Similar to the numerical method in [18], by considering physical meaning, $E_{\mathrm{n}} = -\partial\phi/\partial n$, the weak form of the initial value-boundary value problem in (1) can be written as:

$$\int_{\Omega} \nabla N_i \bullet \gamma \nabla \varphi \mathrm{d}\Omega + \frac{\partial}{\partial t}\int_{\Omega} \nabla N_i \bullet \varepsilon \nabla \varphi \mathrm{d}\Omega = -\int_{\Gamma_{\mathrm{D}}} N_i \gamma E_{\mathrm{n}} \mathrm{d}\Gamma - \frac{\partial}{\partial t}\int_{\Gamma_{\mathrm{D}}} N_i \varepsilon E_{\mathrm{n}} \mathrm{d}\Gamma \tag{2}$$

where Ω is the field domain, Γ_{D} is the Dirichlet boundary illustrated in Fig. 4, N_i is the nodal basis function at node i, E_{n} is the normal component of the electric field intensity.

Compared to the traditional nodal finite element method, the integration of the normal component of the electric field on the Dirichlet boundary is considered in right end of (2) which can be solved in (2).

In the calculation, the rise time and the fall time of the PPSW voltage are several microseconds, therefore, the drastic change of the applied voltage may cause the numerical oscillation. To eliminate numerical oscillation, the Backward-Euler method is selected for the time difference [30]. Therefore, after discretization of time, the weak form (2) can be expressed as the matrix form:

$$\boldsymbol{S}\boldsymbol{\Phi}^{(n+1)} = \boldsymbol{T}\boldsymbol{\Phi}^{(n)} + \boldsymbol{G}^{(n)} + \boldsymbol{F}^{(n+1)}, \tag{3}$$

where $\boldsymbol{S}$ and $\boldsymbol{T}$ are stiffness matrixes, $\boldsymbol{G}$ and $\boldsymbol{F}$ are column vectors related to the E_{n} on the Dirichlet boundary, superscript (n) and $(n+1)$ stand for time step n and $(n+1)$, and $\boldsymbol{\Phi}$ is the column vector of the nodal potential.

Due to the symmetry of the submodule and the homogeneous Neumann boundary of the model, which are depicted in the green line in Fig. 4, elements in $\boldsymbol{G}$ and $\boldsymbol{F}$ are zero except for the nodes on the Dirichlet boundary. When numbering the nodes, nodes that in Ω but not on the Γ_{D} are numbered first. Then, nodes on the Γ_{D} with given nodal potentials are numbered in sequence. Therefore, (3) can be represented as the partitioned matrices form,

$$\begin{bmatrix} \boldsymbol{S}_{11} & \boldsymbol{S}_{21}^{\mathrm{T}} \\ \boldsymbol{S}_{21} & \boldsymbol{S}_{22} \end{bmatrix} \begin{bmatrix} \boldsymbol{\Phi}^{(n+1)} \\ \boldsymbol{U}^{(n+1)} \end{bmatrix} = \begin{bmatrix} \boldsymbol{T}_{11} & \boldsymbol{T}_{21}^{\mathrm{T}} \\ \boldsymbol{T}_{21} & \boldsymbol{T}_{22} \end{bmatrix} \begin{bmatrix} \boldsymbol{\Phi}^{(n)} \\ \boldsymbol{U}^{(n)} \end{bmatrix} + \begin{bmatrix} 0 \\ \boldsymbol{G}^{(n)} \end{bmatrix} + \begin{bmatrix} 0 \\ \boldsymbol{F}^{(n+1)} \end{bmatrix}, \tag{4}$$

where $\boldsymbol{\Phi}$ is a column vector of the nodal potential which is needed to be solved, $\boldsymbol{U}$ is a column vector of the nodal potential with known values on the Dirichlet boundary, Equation (4) can be decomposed into the following two matrix equations,

$$\boldsymbol{\Phi}^{(n+1)} = \boldsymbol{S}_{11}^{-1}(\boldsymbol{T}_{11}\boldsymbol{\Phi}^{(n)} + \boldsymbol{T}_{21}^{\mathrm{T}}\boldsymbol{U}^{(n)} - \boldsymbol{S}_{21}^{\mathrm{T}}\boldsymbol{U}^{(n+1)}) \tag{5}$$

$$\boldsymbol{F}^{(n+1)} = \boldsymbol{S}_{21}\boldsymbol{\Phi}^{(n+1)} + \boldsymbol{S}_{22}\boldsymbol{U}^{(n+1)} - \boldsymbol{T}_{21}\boldsymbol{\Phi}^{(n)} - \boldsymbol{T}_{22}\boldsymbol{U}^{(n)} - \boldsymbol{G}^{(n)} \tag{6}$$

The time-domain finite element equation (5) can solve the transient nodal potential step by step. Due to the different boundary conditions in different working states, the dimension of (5) is different. As illustrated in Fig. 4, the die is simplified as a conductor when at the on-state, and the nodal potential in the die is zero, which does not need to be solved. While during the turn-off process, the turn-on process, and at the off-state, the die is considered as the dielectrics, therefore, the potential inside of the die needs to be calculated. As a result, the dimension of $\boldsymbol{\Phi}$ is decreased compared to the state of the turn-off process, the turn-on process, and the off-state. And the decreased dimension is equal to the number of nodes inside the die. In addition, the corresponding $\boldsymbol{S}_{11}$, $\boldsymbol{S}_{21}$, $\boldsymbol{T}_{11}$, and $\boldsymbol{T}_{21}$ in (5) at the turn-on state also excludes nodes inside the die.

Equation (6) is the transient constrained electric field equation on the boundary (TCEFEB) which contains the E_{n} on the Dirichlet boundary. By using Galerkin's finite element method for the E_{n} on the Dirichlet boundary, E_{n} can be solved as:

$$\boldsymbol{E}_{\mathrm{n}}^{(n+1)} = -\boldsymbol{K}^{-1}(\boldsymbol{S}_{21}\boldsymbol{\Phi}^{(n+1)} + \boldsymbol{S}_{22}\boldsymbol{U}^{(n+1)} - \boldsymbol{T}_{21}\boldsymbol{\Phi}^{(n)} - \boldsymbol{T}_{22}\boldsymbol{U}^{(n)} - \boldsymbol{H}\boldsymbol{E}_{\mathrm{n}}^{(n)}) \tag{7}$$

where $\boldsymbol{K}$ and $\boldsymbol{H}$ are stiffness matrixes corresponding to $\boldsymbol{G}$ and $\boldsymbol{F}$ on the Dirichlet boundary.

To solve E_{n} on the three dielectric interfaces which are shown in Fig. 2, the filed domain Ω needs to be decomposed into four subdomains with only one material. Then, all the dielectric interfaces between subdomain Ω_i $(i = 1, 2, 3, 4)$ and

other subdomains and the Dirichlet boundary of subdomain Ω_i are regarded as the equivalent Dirichlet boundary. Therefore, $E_{\rm n}$ on the equivalent Dirichlet boundary of subdomain Ω_i at each time step can be calculated by (7). It is worth noting that the $\boldsymbol{S}$ and $\boldsymbol{T}$ are stiffness matrixes in subdomain Ω_i. The dimension of the $\boldsymbol{S}_{21}$, $\boldsymbol{S}_{22}$, $\boldsymbol{T}_{21}$, and $\boldsymbol{T}_{22}$ in (7) are the number of nodes on the equivalent Dirichlet boundary of subdomain Ω_i. Repeating the above procedures for four subdomains, $E_{\rm n}$ at each time step on the Dirichlet boundary and both sides of the dielectric interface of domain Ω can be solved.

The transient interfacial charge density $\sigma_{\rm s}$ on the dielectric interfaces Γ_{ij} can be calculated by [15]:

$$\sigma_{\rm s} = \varepsilon_j E_{j\rm n} - \varepsilon_i E_{i\rm n}, \tag{8}$$

where ε_i and ε_j are permittivities in subdomain Ω_i and Ω_j respectively, $E_{i\rm n}$ and $E_{j\rm n}$ are the normal components of the electric field on the interface Γ_{ij} at a different side of subdomain Ω_i and Ω_j, respectively.

For interface 2 and interface 3, which are depicted in Fig. 2, the transient interfacial charge density can be solved by (8) step by step. For interface 1, when during the turn-off process, the turn-on process, and at the off-state, the transient interfacial charge density also can be calculated by (8). While at the turn-on process, the die is the conductor, and interface 1 is the Dirichlet boundary. As a result, the transient interfacial charge density on interface 1 at the turn-on process is equal to the normal component of the electric flux on interface 1 at the passive layer side.

B. Verification of Numerical Method

To testify the validity of the calculation method and our calculation program, a classical model with double-layered dielectrics in series is selected, as shown in Fig. 5. Dielectrics in the model are isotropic linear and homogeneous, which are labeled as 1 and 2. For the dielectric 1, the thickness, the permittivity, and the conductivity are d_1, ε_1, and γ_1, respectively, while for the dielectric 2, these parameters are d_2, ε_2, and γ_2, respectively. When $t = 0$, the switch is closed and the voltage $u_s(t)$ is applied across the two electrodes. The fringing effect is neglected, thus the fields in each dielectric are uniform [15].

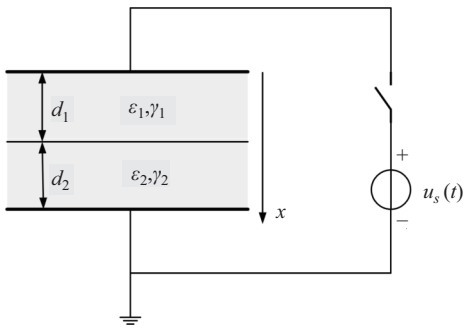

Fig. 5. Model of the double-layer dielectric composite structure.

As illustrated in Fig. 3, if the rise time $t_{\rm r}$ and the fall time $t_{\rm f}$ of the PPSW voltage is 0, the voltage is the ideal PPSW voltage. If the applied voltage $u_s(t)$ is the ideal PPSW voltage, the electric field intensity and the interfacial charge density of the model depicted in Fig. 5 are analytical.

Under the ideal PPSW voltage, the numerical results of the electric field intensity and the interfacial charge density are compared with the analytical solution in Fig. 6. In the calculation, $d_1 = d_2 = 1$ mm, $\varepsilon_{r1} = 3.93$, $\gamma_1 = 2.55 \times 10^{-15}$ S/m, $\varepsilon_{r2} = 2.78$, and $\gamma_2 = 1.04 \times 10^{-12}$ S/m, $U_{\rm m} = 1$ kV, $T = 100$ s, $\alpha = 0.5$. In addition, the total calculation time is 300 s, and the time step is 0.5 s. As shown in Fig. 6, the numerical solution of the electric field intensity and the interfacial charge density are in good agreement with the analytical solution. Therefore, the results show the proposed calculation method is effective.

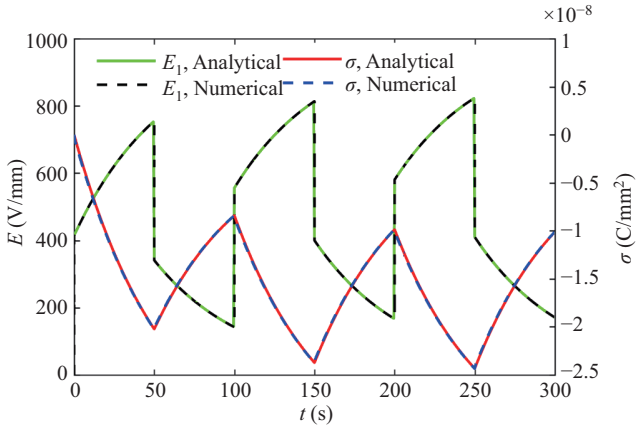

Fig. 6. Comparison of analytical and numerical results of the electric field intensity and the interfacial charge density.

IV. Characterization of Transient Electric Field

In this section, transient characterizations of the electric field and interface charge density under the repetitive turn-on and turn-off state are analyzed in detail. The calculation is conducted based on the proposed calculation method and our calculation program. In the calculation, the magnitude of the PPSW voltage is $U_{\rm m} = 3300$ V, the frequency of the voltage is $f = 50$ Hz, the duty cycle is $\alpha = 0.5$, the rise time and fall time of the voltage is $t_{\rm r} = t_{\rm f} = 2$ μs, the total calculation time is 500 s, the total number of cycles is 25,000. These waveform parameters are corresponding to a typical working voltage of a PPI device for the power grid application.

A. Electric Field Varying with Time

To demonstrate an electric field varying with time, the point on the interface between the passive layer and nitrogen of which the horizontal axis is 5.8 mm is selected. The electric field of the selected point varying with time is depicted in Fig. 7.

As shown in Fig. 7, the overall trend of the electric field varying with time is to increase from zero, and eventually trends to stability. In each cycle of the PPSW voltage, the electric field increases during the off-state, and then decreases during the on-state. Thus, the maximum of the electric field appears at the end of the off-state, while the minimum appears at the end of the on-state. The electric field can step change

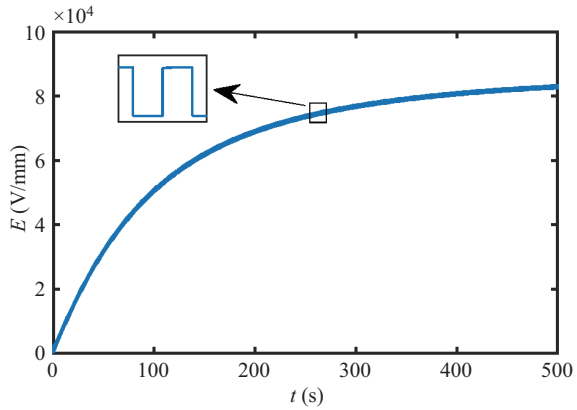

Fig. 7. Electric field varying with time.

with the applied voltage. As a result, the electric field intensity varying with time in a cycle is more likely to be the waveform of the PPSW voltage, which is zoomed in Fig. 7. The electric field at the end of the off-state and the on-state in each cycle will be discussed in detail in the following part.

B. Interfacial Charge Density Varying with Time

The composite insulation structure of the submodule is composed of different insulation materials. Under the working state of the repetitive turn-on and turn-off, interfacial charges will be accumulated on the dielectric interface due to the discontinuity of the permittivity and conductivity on both sides of the interface. The transient characteristics of the interfacial charge density will modify the transient characteristics of the electric field. Therefore, the transient characteristics of the interfacial charge density need to be considered. The interfacial charge density of the selected point is the same as that in Section IV. The interfacial charge density varying with time is depicted in Fig. 8.

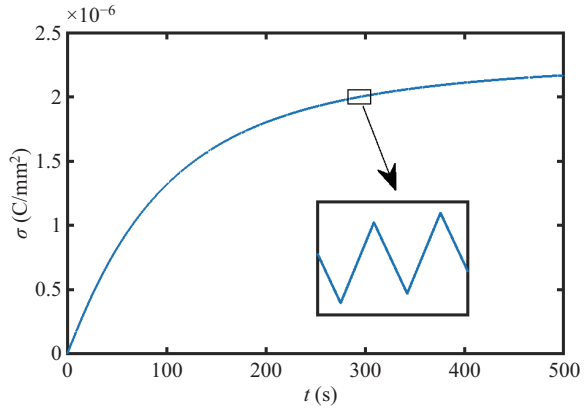

Fig. 8. Interfacial charge density varying with time.

As depicted in Fig. 8, the overall trend of the interfacial charge density varying with time is also to increase from zero, and eventually trends to stability, which is similar to the electric field. However, the interfacial charge cannot sharply change with the applied voltage. Therefore, the interfacial charge density varying with time in a cycle is more likely to be the saw-tooth wave, which is zoomed in Fig. 8.

In each cycle of the PPSW voltage, the composite insulation structure experiences interfacial polarization when $U(t) > 0$, and then experiences interfacial depolarization when $U(t) = 0$. As a result, interfacial charge density will be accumulated during the off-state, and then dissipated during the on-state. In each cycle, the accumulated interfacial charge during the off-state cannot be dissipated completely during the on-state. Therefore, the overall trend of the interfacial charge density is to increase cycle by cycle until it arrives at stabilization.

C. Electric Potential Distribution at the End of the Off-state

To illustrate the transient characterization of the electric field distribution at the end of the off-state in each cycle, the equipotential maps of the submodule at the end of the off-state in the 1st cycle, the 6250th cycle, and the 25000th cycle are given in Fig. 9(a), Fig. 9(b), and Fig. 9(c) respectively.

In the equipotential map, the area with dense equipotential lines indicates the local reinforced electric field. Therefore, three main positions exist with the reinforced electric field located at the surface of the passivation layers, the edge of

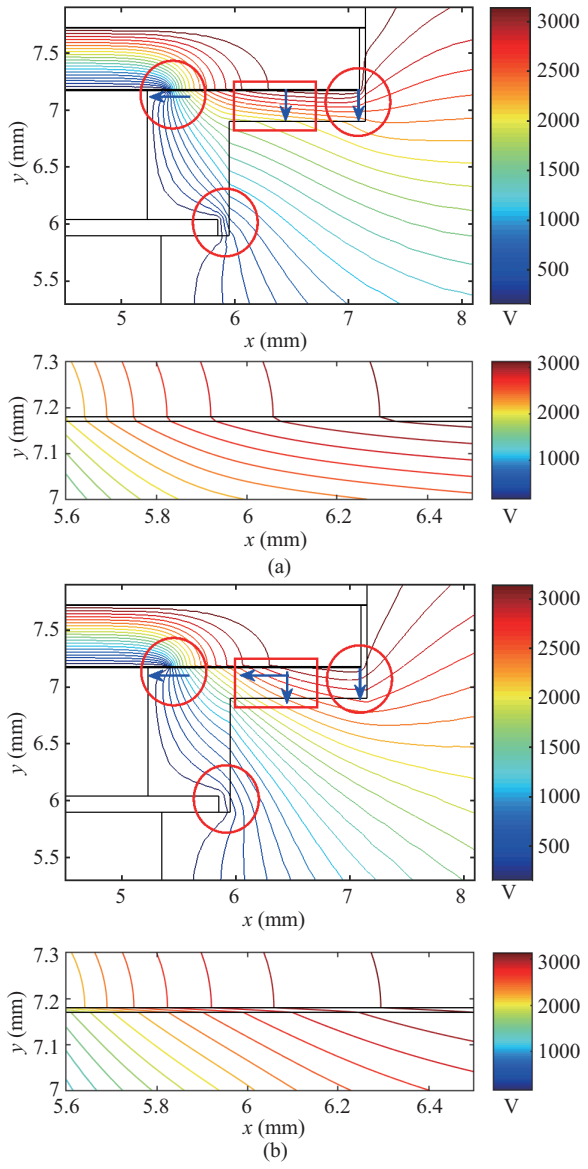

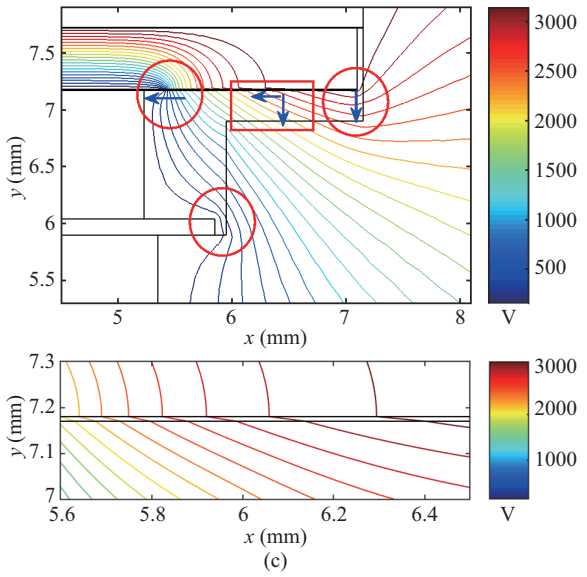

Fig. 9. Distribution of equipotential lines of submodule at the end of off-state in different cycles. (a) In the 1st cycle. (b) In the 6250th cycle. (c) In the 25000th cycle.

the silver plate, and the nitrogen gap between the die and the PEEK frame, which are marked with red cycles in Fig. 9. The reinforced electric field at the surface of the passivation layers is due to the discontinuity of the permittivity and conductivity at the interface of passivation layers and the gas. In addition, the reinforced electric field at the edge of the silver plate is due to the thickness and the curvature of the silver plate. Additionally, the reinforced electric field at the nitrogen gap between the die and the PEEK frame is due to the discontinuity of the dielectric and conduction property of different materials in the region.

Furthermore, the main components of the electric field in these critical areas are marked with blue arrows. The electric field on the surface of the passive layer near the upper molybdenum pad is dominated by the tangential component which is along the negative direction of the x-axis. The electric field in the nitrogen gap between the die and the PEEK frame is dominated by the tangential component which is along the negative direction of the y-axis. Moreover, the module of the electric field in the above three areas decreases as the increase of time for the applied voltage.

In the nitrogen gap between the die and the PEEK frame, which is marked with a red rectangular, the main component of the electric field is the normal component along the negative direction of the x-axis at the first cycle of the voltage. As the increase of time, the normal component decreases gradually, while the tangential component increases gradually. In the last calculation cycle, the electric field is dominated by the tangential component. This transition is due to the charge relaxation phenomenon which will be illustrated in the following section in detail.

D. Electric Field Distribution at the End of On-state

The distribution of the electric field module of submodule at the end of the on-state in the 1st cycle, the 6250th cycle, and the 25000th cycle in three different cycles are depicted in Fig. 10(a), Fig. 10(b), and Fig. 10(c), respectively.

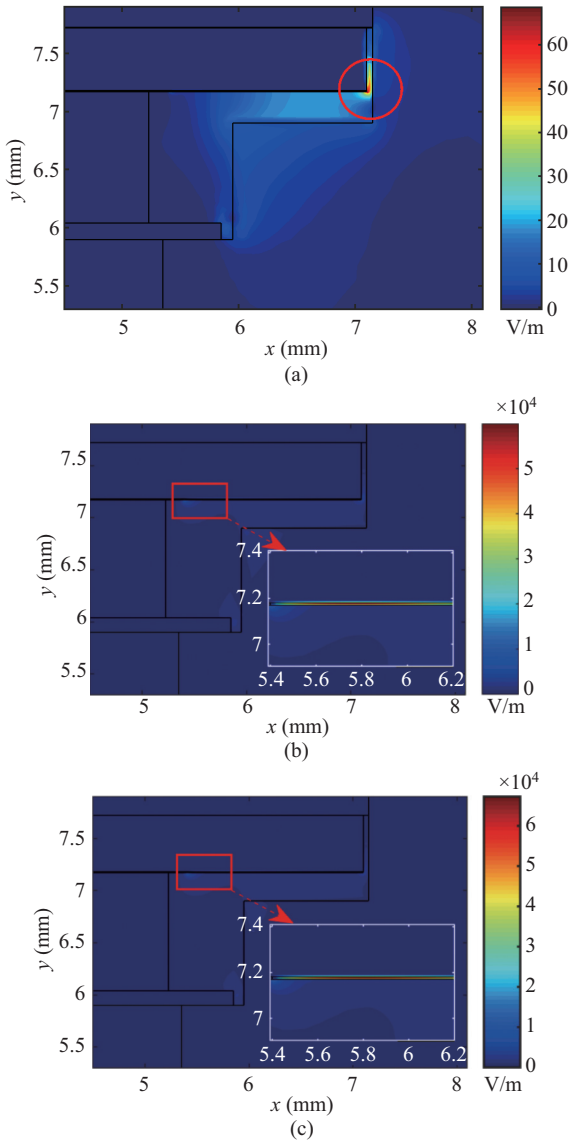

Fig. 10. Field map submodule at the end of on-state in different cycles. (a) In the 1st cycle. (b) In the 12500th cycle. (c) In the 25000th cycle.

Under the on-state, $U(t) = 0$, but the electric field still exists in the package insulation structure. This phenomenon is owing to the effect of the accumulated interface charge. Due to the discontinuity of the permittivity and the conductivity of different materials, charges will gradually accumulate on the dielectric interface when $U(t) > 0$ in each cycle of the PPSW voltage, but during the on-state, the interfacial charge will dissipate. The time constant of the charge relaxation is much large than the duration of the on-state, thus, the accumulated interfacial charge in a cycle cannot be dissipated completely. Therefore, net interfacial charges will be accumulated at the end of each cycle. Accumulated charges generate the electric field which can explain the reason for the above phenomenon.

In the first cycle, the accumulated interfacial charge is very small, thus the module of the electric field is also very small,

as shown in Fig. 10(a). As the number of cycles increases, the magnitude of the accumulated interfacial charge increases. Therefore, the module of the electric field also increases with the increase in the number of cycles, which is depicted in Fig. 10(b) and Fig. 10(c).

E. Maximum Electric Field and Position Varying with Time

The maximum electric field ($E_{\max}$) and the position where it appears at the end of the off-state and on-state in each cycle are illustrated in Fig. 11. As shown in Fig. 11(a), in each cycle, $E_{\max}$ at the end of the off-state occurs on the interface of the die and the passive layer, while on the interface of the passive layer and the nitrogen at the end of the on-state. The vertical ordinate of each point on the above two interfaces are the same, thus, the change of the horizontal ordinate with time can reflect the change of position where $E_{\max}$ occurs with time. The module of $E_{\max}$ and its horizontal ordinate are depicted in Fig. 11(b).

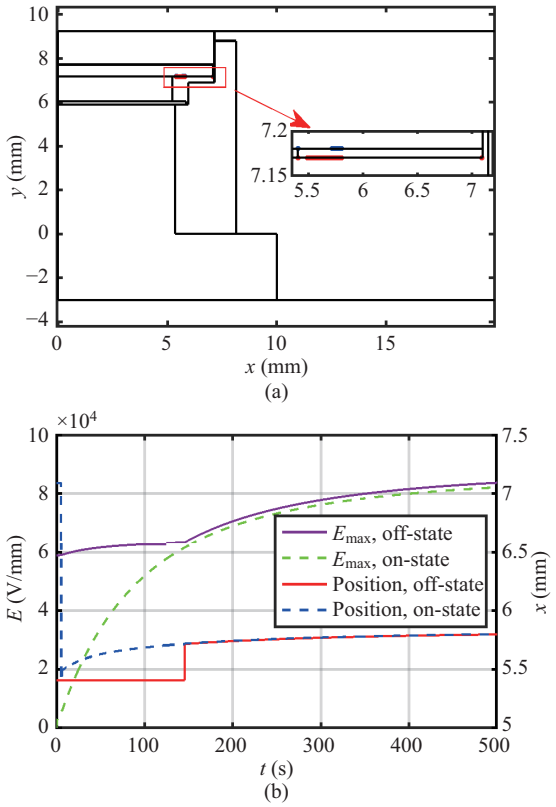

Fig. 11. Maximum electric field and the position where it appears, (a) superposition diagram of the position where the maximum electric field occurs, (b) maximum electric field and it's horizontal ordinate.

As shown in Fig. 11(b), the module of $E_{\max}$ increases with time, moreover, the position where $E_{\max}$ occurs also transfers with time. In the initial stage, only a few charges are accumulated on the dielectric interface, therefore, the electric field introduced by the accumulated charge is much smaller than the field originated by the applied high voltage U_{m}. As a result, $E_{\max}$ at the end of the on-state originated by the accumulated charge is much smaller than $E_{\max}$ at the end of the off-state originated by both the U_{m} and interfacial charge. With the increase of time, the accumulated interfacial charge gradually increases, and the electric field originated by the accumulated charge is comparable with the electric field introduced by U_{m}. When $t > 145$ s, the electric field originated by the accumulated charge is larger than the electric field introduced by the U_{m}. As a consequence, after $t > 145$ s, $E_{\max}$ at the end of the on-state is close to$E_{\max}$ at the end of the off-state, and their difference is the electric field originated by U_{m}.

The position of $E_{\max}$ at the end of the off-state occurs on the interface between the die and the passive layer, while at the end of the on-state $E_{\max}$ occurs on the interface between the passive layer and the nitrogen. When $E_{\max}$ at the end of the off-state is dominated by the U_{m}, the position of $E_{\max}$ occurs at the left edge of the interface. After $t > 145$ s, $E_{\max}$ at the end of the off-state is dominated by the accumulated charge, the position of $E_{\max}$ transfers to the right of the interface with time. While $E_{\max}$ at the end of the on-state occurs at the right edge of the interface in the beginning, then transfers from the left edge to the right along with the interface, which is also depicted in Fig.10 marked with the red cycle. And after $t >$ 145 s, the horizontal position is the same as the $E_{\max}$ on the off-edge.

F. Distribution of Interfacial Charge Density

As shown in Fig. 2, there are three main dielectric interfaces in the calculation model with the local enhanced electric field, the interface between the die and the passive layer, the interface between the passive layer and nitrogen, and the interface between PEEK and nitrogen. The interfacial charge on the above three interfaces is a main concern. In addition, the interfacial charge at the end of the on-state in each cycle reflects the net accumulation of interfacial charge in each cycle.

The distribution of interfacial charge densities at the end of the on-state in different cycles are depicted in Fig. 12, where Fig. 12(a), 12(b), and 12(c) are interfacial charge density on the interface between the die and the passive layer, the interface between passive layer and nitrogen, and the interface between PEEK and nitrogen, respectively. For simplicity, the above three interfaces are labeled as interfaces 1, 2, and 3, respectively. In addition, the reference directions of the normal vector on the above three interfaces are from the passive layer to the die, from nitrogen to the passive layer, and from nitrogen to the PEEK, respectively.

The characteristics of the interfacial charge density on interfaces 1 and 2 share similar trends except for the polarity of the charge, as shown in Fig. 12(a) and Fig. 12(b). The net accumulation of the interfacial charge at each point of the corresponding interface increases with the increase of the number of the cycle. Moreover, the place where the maximum magnitude of the charge density occurs on the interface transfers with time. As the increase of the number of the cycle, the place with the maximum charge density gradually transfers from the left edge of the interface to the right.

As shown in Fig. 12(c), the magnitude of the interfacial charge density on interface 3 is smaller than the magnitude on interfaces 1 and 2. The magnitude of the charge density can reflect the electric field to some extent, therefore, the

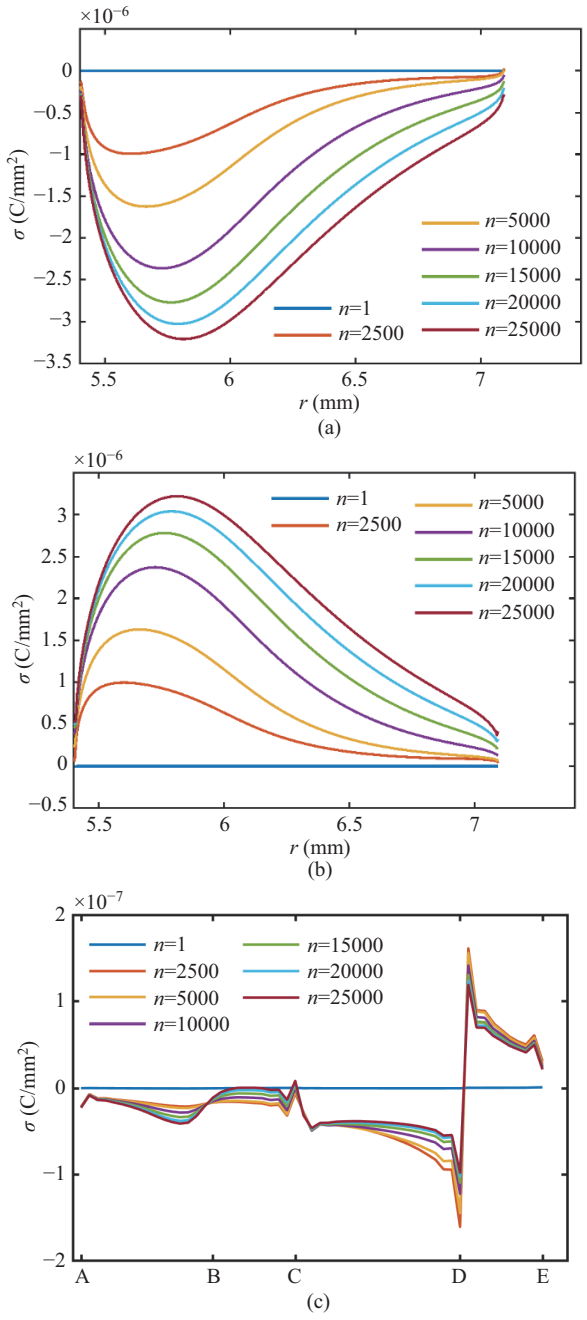

Fig. 12. Distribution of interface charge density at the end of on-state in different cycles. (a) Interface between die and passive layer. (b) Interface between passive layer and nitrogen. (c) Interface between PEEK and nitrogen.

electric field on interface 3 is smaller than interface 1 and 2. For segment AB, the electric field is dominated by the normal component, therefore, the magnitude of the interfacial charge density increases with the increase of the number of the cycle. While for other segments of interface 3, as the increase of the number of the cycles, the tangential component gradually dominates the electric field, but the normal component gradually decreases. As a result, the magnitude of the interfacial charge density decreases with the increase of the number of the cycles. In addition, the maximum magnitude of the interfacial charge density occurs at point D, which indicates the maximum electric field on interface 3. Moreover, the polarity of the interfacial charge changes at point D, which is caused by the choice of the reference direction.

V. Discussions

In this section, the influence of the duty cycle and the repetitive frequency of the PPSW voltage on the electric field and the interfacial charge density will be discussed.

A. The Influence of the Duty Cycle on the Interfacial Charge Density and Electric Field

The characteristics of the interfacial charge density and the electric field of a point under different duty cycles of 0.3, 0.5, 0.7, and 0.9 are depicted in Fig. 13. The selected point is on the interface between the passive layer and nitrogen, and its horizontal axis is 5.8, corresponding to the maximum electric field. In the calculation, other parameters of the voltage are set the same as that in Section IV.

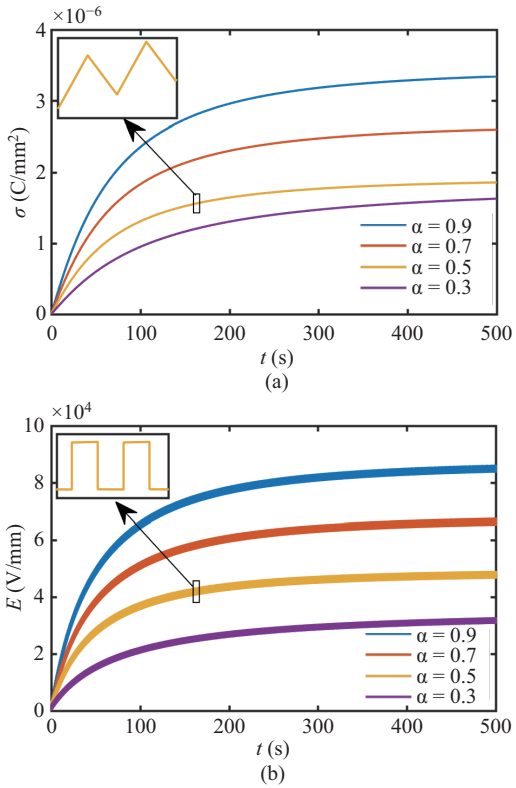

Fig. 13. The influence of the duty cycle to the electric field and the interfacial charge density. (a) Interfacial charge density. (b) Electric field intensity.

As depicted in Fig. 13(a), interfacial charge density increases with the increase of the duty cycle. In addition, the magnitude of the interfacial charge density increases during the off-state in each cycle while decreasing during the on-state. During the off-state, $U(t) = U_{\mathrm{m}}$, the interfacial polarization is experienced, therefore interfacial charges gradually accumulate, while during the on-state, $U(t) = 0$, the interfacial depolarization is experienced, therefore interfacial charges gradually disperse. Therefore, given the same cycle, the larger the duty cycle is, the longer time it takes to experience the polarization process, and the more charges accumulate. At the

same time, the larger the duty cycle is, the shorter time it takes to experience the depolarization process, and the fewer charges disperse. As a result, interfacial charge density increases with the increase of the duty cycle.

The influence of the duty cycle on the electric field intensity is shown in Fig. 13(b). The origin of the electric field can be divided into two parts, one is the applied voltage, and the other is the interfacial charge. During the off-state of each cycle, $U(t) = U_{\mathrm{m}}$, the applied voltage contributes to the electric field. In addition, the electric field originated by the interfacial charge increases due to the increase of the interfacial charge density. Therefore, the electric field gradually increases during the off-state. While during the on-state, $U(t) = 0$, the applied voltage does not contribute to the electric field, the electric field is originated only by the accumulated interfacial charge. Therefore, the electric field decreases during the on-state due to the decrease of the interfacial charge density. With the increase of the duty cycle, the accumulated interfacial charges increase in a cycle. As a consequence, the electric field also increases with the increase of the duty cycle.

B. The Influence of the Repetitive Frequency on the Interfacial Charge Density and Electric Field

The characteristics of the interfacial charge density and the electric field of a point under different frequencies of 0.1 Hz, 1 Hz, 10 Hz, 25 Hz, 50 Hz, and 100 Hz are depicted in Fig. 14. The selected point is the same as it is in Section V-A. In the calculation, other parameters of the voltage are also set as the same as that in Section IV.

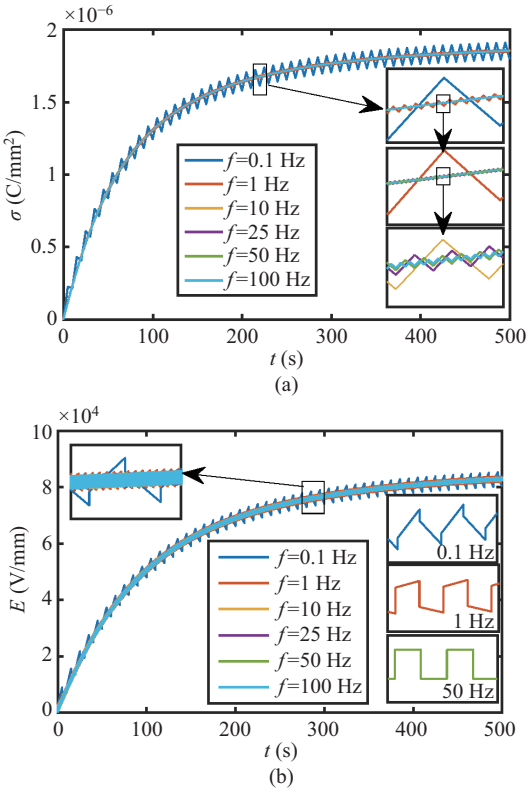

Fig. 14. The influence of the cycle to the electric field and the interfacial charge density. (a) Interfacial charge density. (b) Electric field intensity.

The transient interfacial charge density under different frequencies fluctuates on the same line, as shown in Fig. 14(a). The smaller the frequency is, the larger the cycle is, therefore, the more time it takes to experience the interfacial polarization and the interfacial depolarization when the duty cycle is the same. Therefore, in the same period, the smaller the frequency is, the larger the maximum interfacial charge density is, and the smaller the minimum interfacial charge density is. The electric field shares the same increasing and decreasing trends with the frequency-varying characteristics as the interfacial charge density, as shown in Fig. 14(b).

To quantify the influence of the frequency, the maximum of the electric field under different frequencies are listed in Table II, in which the maximum electric field of 50 Hz is normalized as 1.

TABLE II
MAXIMUM ELECTRIC FIELD UNDER DIFFERENT FREQUENCIES

Frequency (Hz)	Maximum electric field (normalized)
100	0.99996
50	1
25	1.0001
10	1.0003
1	1.0033
0.1	1.0324

The influence of the frequency on the electric field is small, as illustrated in Table II. When the frequency decreases from 50 Hz to 0.1 Hz, which is decreased by 500 times, the maximum electric field only increases by 3.24%. This is because the corresponding cycle of the PPSW voltage is much smaller than the relaxation time constant of the submodule when the frequency ranges from 100 Hz to 0.1 Hz.

In the time-domain calculation, the higher the frequency is, the more iteration steps it needs, therefore, the more computation time it costs. To lower the computation cost, the electric field calculation of the submodule under the state of repetitive turn-off and turn-on is recommended to be conducted with the frequency of 0.1 Hz. Under this condition, the calculation error caused by the reduction of the calculation cost is about 3%, which is acceptable in engineering.

VI. CONCLUSION

The transient electric field analysis of the press-packed IGBT submodule under the working condition of repetitive turn-off and turn-on is conducted. The main conclusions are as follows.

1) There are three main areas with the reinforced electric field: the surface of the passivation layers, the edge of the silver plate, and the nitrogen gap between the die and the PEEK frame. The risk of partial discharge in these areas is a main concern.

2) In the nitrogen gap between the passive layer and the PEEK frame, the normal component dominates the electric field at the first cycle of the voltage. As time increases, the normal component gradually decreases, while the tangential component gradually dominates the electric field. The risk of the surface discharge on the interface of the passive layer and the nitrogen is an area of concern.

3) During the on-state, the magnitude of the applied voltage is zero, but the electric field still exists in the package insulation structure due to the charge accumulation on the dielectric interface. With the increase of the number of the cycles, the net accumulation of the interfacial charges increases, therefore the electric field also increases.

4) The duty cycle and the repetitive frequency can influence the electric field and the interfacial charge density. Compared with the influence from the repetitive frequency, the influence of the duty cycle is more significant. The electric field and the interfacial charge density increases with the increase of the duty cycle.

5) To decrease the computation costs, the electric field calculation of the submodule under the state of repetitive turn-off and turn-on is recommended to be conducted under the frequency of 0.1 Hz. And the calculation error caused by the reduction of the calculation cost is about 3%, which is acceptable in engineering.

REFERENCES

[1] A. Q. Huang, "Power semiconductor devices for smart grid and renewable energy systems," *Proceedings of the IEEE*, vol. 105, no. 11, pp. 2019–2047, Nov. 2017.

[2] B. K. Bose, "Power electronics, smart grid, and renewable energy systems," *Proceedings of the IEEE*, vol. 105, no. 11, pp. 2011–2018, Nov. 2017.

[3] F. Filsecker, R. Alvarez, and S. Bernet, "Comparison of 4.5-kV press-pack IGBTs and IGCTs for medium-voltage converters," *IEEE Transactions on Industrial Electronics*, vol. 60, no. 2, pp. 440–449, Feb. 2013.

[4] Z. Y. Chen, Z. Q. Yu, X. Y. Zhang, T. Y. Wei, G. Lyu, L. Qu, Y. L. Huang, and R. Zeng, "Analysis and experiments for IGBT, IEGT, and IGCT in hybrid DC circuit breaker," *IEEE Transactions on Industrial Electronics*, vol. 65, no. 4, pp. 2883–2892, Apr. 2018.

[5] R. Simpson, A. Plumpton, M. Varley, C. Tonner, P. Taylor, X. P. Dai, "Press-pack IGBTs for HVDC and FACTS," *CSEE Journal of Power and Energy Systems*, vol. 3, no. 3, pp. 302–310, Sep. 2017.

[6] E. P. Deng, Z. B. Zhao, Q. M. Xin, J. W. Zhang, and Y. Z. Huang, "Analysis on the difference of the characteristic between high power IGBT modules and press pack IGBTs," *Microelectronics Reliability*, vol. 78, pp. 25–37, Nov. 2017.

[7] P. Y. Fu, Z. B. Zhao, X. B. Li, X. Cui, T. Wen, Z. D. Yang, S. Y. Mo, and P. Zhang, "Partial discharge measurement and analysis in PPIs," *IET Power Electronics*, vol. 12, no. 1, pp. 138–146, Jan. 2019.

[8] P. Y. Fu, Z. B. Zhao, X. Cui, T. Wen, H. Y. Wang, X. B. Li, P. Zhang, "Partial discharge measurement and analysis in high voltage IGBT modules under DC voltage," *CSEE Journal of Power and Energy Systems*, vol. 4, no. 4, pp. 513–523, Dec. 2018.

[9] M. Ghassemi, "Accelerated insulation aging due to fast, repetitive voltages: A review identifying challenges and future research needs," *IEEE Transactions on Dielectrics and Electrical Insulation*, vol. 26, no. 5, pp. 1558–1568, Oct. 2019.

[10] M. Ghassemi, "PD measurements, failure analysis, and control in high-power IGBT modules," *IET High Voltage*, vol. 3, no. 3, pp. 170–178, Sep. 2018.

[11] A. Nami, J. Q. Liang, F. Dijkhuizen, and G. D. Demetriades, "Modular multilevel converters for HVDC applications: review on converter cells and functionalities," *IEEE Transactions on Power Electronics*, vo. 30, no. 1, pp. 18–36, Jan. 2015.

[12] N. Flourentzou, V. G. Agelidis, and G. D. Demetriades, "VSC-based HVDC power transmission systems: an overview," *IEEE Transactions on Power Electronics*, vol. 24, no. 3, pp. 592–602, Mar. 2009.

[13] F. Wakeman, W. Findlay, and G. R. Li, "Press-pack IGBTs, semiconductor switches for pulse power," in *PPPS-2001 Pulsed Power Plasma Science 2001. 28th IEEE International Conference on Plasma Science and 13th IEEE International Pulsed Power Conference. Digest of Papers* (*Cat. No. 01CH37251*), 2001, pp. 1051–1054.

[14] M. J. Melfi, "Low-Voltage PWM inverter-fed motor insulation issues," *IEEE Transactions on Industry Applications*, vol. 42, no. 1, pp. 128–133, Jan./Feb. 2006.

[15] H. A. Haus and J. R. Melcher, *Electromagnetic Fields and Energy*, Englewood Cliffs, NJ: Prentice-Hall, 1989.

[16] H. K. Dirks, "Quasi-stationary fields for microelectronic applications," *Electrical Engineering*, vol. 79, no. 2, pp. 145–155, Nov. 1996.

[17] L. Egiziano, V. Tucci, C. Petrarca, and M. Vitelli, "A Galerkin model to study the field distribution in electrical components employing nonlinear stress grading materials," *IEEE Transactions on Dielectrics and Electrical Insulation*, vol. 6, no. 6, pp. 765–773, Dec. 1999.

[18] T. Wen, X. Cui, X. B. Li, H. Ma, and Z. B. Zhao, "Time-domain finite element method for transient electric field and transient charge density on dielectric interface," *CSEE Journal of Power and Energy Systems*, vol. 8, no. 1, pp. 143–154, Jan. 2022.

[19] G. Mitic and G. Lefranc, "Localization of electrical-insulation and partial-discharge failures of IGBT modules," *IEEE Transactions on Industry Applications*, vol. 38, no. 1, pp. 175–180, Jan./Feb. 2002.

[20] D. Frey, J. L. Schanen, J. L. Auge, and O. Lesaint, "Electric field investigation in high voltage power modules using finite element simulations and partial discharge measurements," in *38th IAS Annual Meeting on Conference Record of the Industry Applications Conference*, 2003, pp. 1000–1005.

[21] J. H. Fabian, S. Hartmann, and A. Hamidi, "Analysis of insulation failure modes in high power IGBT modules," in *Fourtieth IAS Annual Meeting. Conference Record of the 2005 Industry Applications Conference*, 2005, pp. 799–805.

[22] L. Donzel and J. Schuderer, "Nonlinear resistive electric field control for power electronic modules," *IEEE Transactions on Dielectrics and Electrical Insulation*, vol. 19, no. 3, pp. 955–959, Jun. 2012.

[23] C. F. Bayer, E. Baer, U. Waltrich, D. Malipaard, and A. Schletz, "Simulation of the electric field strength in the vicinity of metallization edges on dielectric substrates," *IEEE Transactions on Dielectrics and Electrical Insulation*, vol. 22, no. 1, pp. 257–265, Feb. 2015.

[24] M. M. Tousi and M. Ghassemi, "Combined geometrical techniques and applying nonlinear field dependent conductivity layers to address the high electric field stress issue in high voltage high-density wide bandgap power modules," *IEEE Transactions on Dielectrics and Electrical Insulation*, vol. 27, no. 1, pp. 305–313, Feb. 2020.

[25] M. M. Tousi and M. Ghassemi, "Characterization of nonlinear field-dependent conductivity layer coupled with protruding substrate to address high electric field issue within high-voltage high-density wide bandgap power modules," *IEEE Journal of Emerging and Selected Topics in Power Electronics*, vol. 8, no. 1, pp. 343–350, Mar. 2020.

[26] P. Y. Fu, Z. B. Zhao, X. Cui, P. Zhang, and R. G. Han, "Electrical field analysis of press-pack IGBTs," in *2017 Sixth Asia-Pacific Conference on Antennas and Propagation* (*APCAP*), 2017, pp. 1–3.

[27] J. Y. Li, J. D. Sun, Z. B. Zhao, P. Zhang, and N. W. Guo, "Study on the issue of electric field concentration in submodule of press pack IGBTs," in *2017 Sixth Asia-Pacific Conference on Antennas and Propagation* (*APCAP*), 2017, pp. 1–3.

[28] M. M. Tousi and M. Ghassemi, "The effect of type of voltage (sinusoidal and square waveform) and the frequency on the performance of nonlinear field-dependent conductivity coatings for electric field control in power electronic modules," in *2019 IEEE Conference on Electrical Insulation and Dielectric Phenomena* (*CEIDP*), 2019, pp. 552–555.

[29] M. Sweet, E. S. Sankara Narayanan, and S. Steinhoff, "Influence of cassette design upon breakdown performance of a 4.5kV press-pack IGBT module," in *8th IET International Conference on Power Electronics, Machines and Drives* (*PEMD 2016*), Glasgow, UK, 2016, pp. 1–6.

[30] J. R. Marti and J. M. Lin, "Suppression of numerical oscillations in the EMTP," *IEEE Power Engineering Review*, vol. 9, no. 5, pp. 71–72, May 1989.

Teng Wen received a B.Sc. degree in Electrical Engineering from North China Electric Power University, Beijing, China, in 2013. He is currently a Ph.D. candidate in Electrical Engineering at North China Electric Power University. His main research interests include computational electromagnetics, electrical insulation, and packaging problems for high voltage power semiconductor devices.

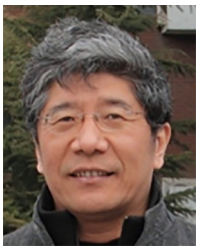

Xiang Cui (M'97–SM'98) received B.Sc. and M.Sc. degrees in Electrical Engineering from North China Electric Power University, Baoding, China, in 1982 and 1984, respectively, and a Ph.D. degree in Accelerator Physics from the China Institute of Atomic Energy, Beijing, China, in 1988. He is currently a Professor and the Vice Director of the State Key Laboratory of Alternate Electrical Power Systems with Renewable Energy Sources, North China Electric Power University. His research interests include computational electromagnetics, electromagnetic environment, and electromagnetic compatibility in power systems, insulation, and magnetic problems in high-voltage apparatus. Prof. Cui is a Standing Council Member of the China Electrotechnical Society, a Fellow of IET, a Senior Member of IEEE. He is also an Associate Editor of *IEEE Transactions on Electromagnetic Compatibility*.

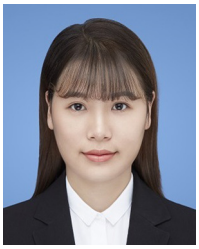

Sijia Liu received a B.Sc. degree in Electrical engineering from North China Electric Power University, Beijing, China, in 2020, where she is currently pursuing an M.Sc. degree in Electrical Engineering. Her main research interests are computational electromagnetics, electrical insulation, and packaging problems for high voltage power semiconductor devices.

Xuebao Li received B.Sc. and Ph.D. degrees in Electrical Engineering from North China Electric Power University, Beijing, China, in 2011 and 2016, respectively. He is currently an Associate Professor at the School of Electrical and Electronic Engineering, North China Electric Power University. His research interests include the electromagnetic environment and electromagnetic compatibility in power systems, and insulation problems in high-voltage apparatus.

Zhibin Zhao received a Ph.D. degree in Electrical Engineering from North China Electric Power University, Baoding, China, in 2005. Currently, he is a Professor at the State Key Laboratory of Alternate Electrical Power System with Renewable Energy Sources, North China Electric Power University. His main research interests include computational electromagnetics and electromagnetic compatibility in power electronics.